UC Berkeley

Title
Manganese–Cobalt Oxido Cubanes Relevant to Manganese-Doped Water Oxidation Catalysts

Authors
Nguyen, Andy I
Suess, Daniel LM
Darago, Lucy E
et al.

Manganese–Cobalt Oxido Cubanes Relevant to Manganese-Doped Water Oxidation Catalysts

Andy I. Nguyen[†,ID], **Daniel L. M. Suess**[‡], **Lucy E. Darago**[†], **Paul H. Oyala**[‡], **Daniel S. Levine**[†,ID], **Micah S. Ziegler**[†,ID], **R. David Britt**[*,‡], and **T. Don Tilley**[*,†]

[†]Department of Chemistry, University of California at Berkeley, Berkeley, California 94720-1460, United States

[‡]Department of Chemistry, University of California at Davis, Davis, California 95616, United States

Abstract

Incorporation of Mn into an established water oxidation catalyst based on a $Co(III)_4O_4$ cubane was achieved by a simple and efficient assembly of permanganate, cobalt(II) acetate, and pyridine to form the cubane oxo cluster $MnCo_3O_4(OAc)_5py_3$ (OAc = acetate, py = pyridine) (**1-OAc**) in good yield. This allows characterization of electronic and chemical properties for a manganese center in a cobalt oxide environment, and provides a molecular model for Mn-doped cobalt oxides. The electronic properties of the cubane are readily tuned by exchange of the OAc^- ligand for Cl^- (**1-Cl**), NO_3^- (**1-NO$_3$**), and pyridine (**[1-py]**$^+$). EPR spectroscopy, SQUID magnetometry, and DFT calculations thoroughly characterized the valence assignment of the cubane as $[Mn^{IV}Co^{III}_3]$. These cubanes are redox-active, and calculations reveal that the Co ions behave as the reservoir for electrons, but their redox potentials are tuned by the choice of ligand at Mn. This $MnCo_3O_4$ cubane system represents a new class of easily prepared, versatile, and redox-active oxido clusters that should contribute to an understanding of mixed-metal, Mn-containing oxides.

Graphical abstract

[*]**Corresponding Authors**. rbritt@ucdavis.edu, tdtilley@berkeley.edu.

ORCID

Andy I. Nguyen: 0000-0003-4137-6453

Daniel S. Levine: 0000-0001-8921-3659
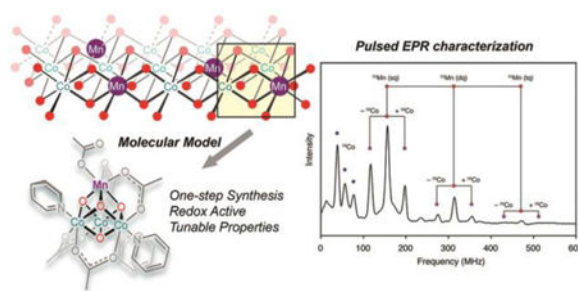
Micah S. Ziegler: 0000-0002-8549-506X

INTRODUCTION

Oxide catalysts for the oxygen-evolution reaction (OER) are of great interest as the essential water-splitting component in artificial photosynthesis.[1] Investigations into the optimization of these catalysts show that they are often more active after doping with a metal impurity or additive.[2,3] For example, this effect is observed in the enhanced OER catalysis that results from doping Mn into CoO_x or Fe into NiO_x.[4,5] This theme extends to Nature where the oxygen-evolving center (OEC) in photosystem II is a mixed calcium–manganese oxido cluster.[6,7] These observations suggest that there are cooperative effects that influence OER mechanisms in heterometallic systems, but the origins of such effects are not well understood. There is therefore a glaring need for in-depth structural, electronic, and mechanistic studies on well-defined heterometallic oxido systems related to those identified as OER catalysts.

The development of appropriate structural models for heterogeneous OER catalysts and Nature's OEC is a longstanding research goal that has provided important information regarding structure–function relationships.[8–14] Functional models that are structurally similar to the OEC, or to an active site of an oxide catalyst, are far more rare. Only recently was the catalytic edge site of the layered oxide–hydroxide CoOOH successfully modeled by the molecular tetracobalt oxido cubane $Co_4(\mu_3\text{-O})_4(OAc)_4py_4$, to reveal a surprising mechanism for OER that implicates an unusually high formal oxidation state for cobalt.[10] Given this conceptual underpinning, it is of interest to establish related, multimetallic models that might provide insights into the origins of the heterometallic cooperative effects.

While the study of heterometallic model oxido clusters could immensely facilitate understanding of more complex OER systems, this endeavor is severely limited by the lack of rational synthetic routes to suitable mixed-metal species. In particular, the selective introduction of oxo ligands (O^{2-}) is quite challenging, given their high basicity and multiple bonding modes, and the lack of reliable synthetic reagents for introduction of this ligand. The precise incorporation of a heterometallic (M–O–M′) linkage into a heterometallic oxido cluster presents an additional, significant synthetic challenge. For these reasons, many of the known examples of molecular metal oxido clusters were initially discovered via serendipitous self-assembly rather than by a designed approach.[12,13,15–18] Furthermore, the postsynthetic modification of oxido clusters is not a well-established approach for probing the influence of structure on electronic and chemical properties. A notable exception is the work of Agapie and co-workers, who have made significant progress toward the rational

synthesis and postsynthetic modification of several metal oxido clusters supported by a trialkoxide ligand.[8,9,19–22] While this approach has provided homo- and heterometallic oxido clusters, the necessity of the chelating trialkoxide ligand is a constraint on the bonding and reactivity of these complexes.

This contribution describes the first syntheses of mixed manganese–cobalt oxido cubanes using a rational approach. These [MnCo$_3$O$_4$] cubanes may be regarded as Mn-doped versions of the [Co$_4$O$_4$] cubane OER catalyst, and may serve as useful models for Mn-doped CoO$_x$ (Figure 1).[10] The new [MnCo$_3$O$_4$]-based clusters are ligated by simple air- and water-stable carboxylate and pyridine ligands, and ligand exchange reactions allow systematic modifications of the Mn coordination sphere. Thus, this work introduces a highly useful, yet easily accessible, motif for studying mixed-metal oxides. The synthetic methods used to obtain these clusters demonstrate design principles for furthering molecular metal–oxido chemistry. The structural and spectroscopic studies of the clusters described herein suggest an [Mn^{IV}Co^{III}$_3$] electronic structure. Significant hyperfine coupling is observed between the $S = 3/2$ Mn(IV) center and the ^{59}Co(III) nuclei, and a further one-electron oxidation is proposed to occur at the Co centers.

RESULTS AND DISCUSSION

Synthesis and Structure

The oxidation states and the stoichiometries of the manganese and cobalt starting materials were adjusted to target a 1:3 Mn:Co ratio for the cluster. Specifically, permanganate (MnO$_4$$^-$) with its Mn(VII) oxidation state was used as a source of the four oxo ligands of the cubane core and to oxidize 3 equiv of Co(II) to Co(III) with concurrent reduction to Mn(IV). Indeed, 3 equiv of cobalt(II) acetate tetrahydrate reacted with potassium permanganate in the presence of pyridine to afford the tetrametallic oxido cluster MnCo$_3$O$_4$(OAc)$_5$py$_3$ (**1-OAc**) in 52% isolated yield as black-brown crystals (Scheme 1). The molecular composition of **1-OAc** was determined by high-resolution electrospray ionization mass spectrometry (HR-ESI-MS) ($m/z = 850.90$, [MnCo$_3$O$_4$(OAc)$_5$py$_3$Na]$^+$). Single-crystal X-ray diffraction (XRD) confirmed **1-OAc** as a C_s-symmetric oxo-cubane, with three Co(III) ions and one Mn(IV), each in a pseudo-octahedral ligand environment at the four corners of the [MnCo$_3$O$_4$]$^{5+}$ core (Figure 1). The somewhat shorter average metal–oxo bond distances associated with one metal center (1.859(2) Å) identify it as the Mn(IV) ion, while the average Co–O(oxo) distance is 1.875(1) Å. Four μ_2-acetate ligands cap four equatorial faces of the cubane, and the fifth acetate is bound to Mn(IV) in a monodentate manner, in an "axial" position of the cubane. Notably, the average Mn–O(μ_2-acetate) distances of 1.992(3) Å are *longer* than the average Co–O(μ_2-acetate) distance of 1.933(3) Å. This difference between the Mn–O(μ_2-acetate) and Co–O(μ_2-acetate) bond lengths may be rationalized by the stronger Mn–O(oxo) versus Co–O(oxo) bond (*vide supra*), giving rise to a stronger *trans*-influence on the Mn–O(μ_2-acetate) bonds. Finally, three pyridine ligands on the axial faces of the cubane complete the coordination spheres of the three Co(III) ions. Notably, **1-OAc** is quite soluble and stable in water and organic solvents such as dichloromethane, acetonitrile, and methanol. Aqueous conductivity measurements of dissolved **1-OAc** do not indicate

ionization at 25 °C, presumably due to the strong ligand-field stabilization of both the t_{2g}^6 and t_{2g}^3 electron configurations of Co(III) and Mn(IV), respectively.

The site-differentiation of the Mn(IV) site allows the monodentate acetate ligand of **1-OAc** to be cleanly and predictably substituted for other ligands. Efficient exchange of the acetate ligand for chloride was achieved by reaction of **1-OAc** with oxalyl chloride, to afford **1-Cl** in 90% yield (Scheme 1). Single-crystal XRD confirmed formation of the chloride complex and provided a Mn–Cl bond length of 2.270(2) Å (Figure 2). The bond distances within the cubane core are nearly identical to those of **1-OAc**. The chloride derivative **1-Cl** is a useful starting point for further ligand substitutions via precipitation of metal chloride salts. For example, exchange for nitrate (NO_3^-) upon reaction of **1-Cl** with silver nitrate produced **1-NO$_3$** (Scheme 1). The structure of **1-NO$_3$** (Figure 2) reveals a slight contraction of the Mn–O bond *trans* to the nitrate, from 1.864(4) Å in **1-OAc** to 1.846(4) Å, which is consistent with weaker σ-donation and a lower *trans*-influence for nitrate and a concomitant strengthening of the Mn–O(oxo) bond. The average Co–O bond lengths remain essentially unchanged through these substitutions.

The strong acid 4-toluenesulfonic acid (HOTs) reacted with **1-OAc** by way of exchange of an acetate ligand for tosylate (OTs), driven by formation of acetic acid, to generate **1-OTs** in 100% yield. The cubane bond metrics, determined by single crystal XRD, are similar to those of **1-NO$_3$** and are consistent with the low Lewis basicity of 4-toluenesulfonate. Generation of a cationic species was achieved by displacement of the monodentate acetate ligand of Mn(IV) in **1-OAc** with a neutral pyridine ligand. Upon heating an aqueous solution of **1-OAc** with excess pyridine in the presence of hexafluorophosphate anion (PF_6^-), the complex [Co$_3$MnO$_4$(OAc)$_4$py$_4$]PF$_6$, **[1-py]PF$_6$**, precipitated as dark brown crystals (43%). Compound **[1-py]PF$_6$** crystallizes in the $C2/c$ space group, resulting in substitutional disorder of the Co and Mn atoms; however, HR-ESI-MS unambiguously established the molecular composition (m/z = 847.94, [Co$_3$MnO$_4$(OAc)$_4$py$_4$]$^+$). It is noteworthy that **[1-py]PF$_6$** is isostructural, but not isoelectronic, with the previously described all-cobalt derivative [Co$_4$O$_4$(OAc)$_4$py$_4$]$^+$.[10,11,23]

Redox Chemistry

Complex **1-OAc** exhibits a quasi-reversible redox couple in the cyclic voltammogram (CV) at $E_{1/2} \approx 1.15$ V (all potentials are referenced against Fc/Fc$^+$) and a second reversible redox event at $E_{1/2} \approx 1.49$ V. With increasing scan rates ($v > 0.10$ V/s), the anodic and cathodic peak currents of the 1.15 V couple grow to about twice those associated with the 1.49 V couple. The plot of normalized current versus potential clearly demonstrates that the 1.15 V redox couple becomes more chemically reversible (i_a/i_p approaches unity) at faster scan rates, while the 1.49 V redox couple diminishes in current (Figures 3A and 3B). This suggests that the electrochemical event at 1.15 V is followed by a chemical reaction, to produce a daughter species with a redox couple at 1.49 V (ECE mechanism). The first electrochemical event is assigned as a one-electron couple for [MnCo$_3$O$_4$]$^{5+}$/[MnCo$_3$O$_4$]$^{6+}$. The derivatives **1-Cl**, **1-NO$_3$**, and **[1-py]$^+$** exhibit only one redox event at a potential similar to that of the first redox event for **1-OAc**, but are more positively shifted. The ranking of clusters with respect to $E_{1/2}$ redox potential (lowest to highest) is **1-OAc** (1.15 V), **1-Cl**

(1.18 V), **1-NO₃** (~1.2 V), and **[1-py]**⁺ (1.48 V) (Figure 3A). This ranking correlates with the magnitude of the electrostatic interaction between the monodentate ligand and Mn: more basic ligands are more effective in stabilizing the oxidized cluster.[24] The reversibility of the redox couple for **1-NO₃** is noteworthy, in that it is completely irreversible at $v \leq 100$ mV/s but becomes almost fully reversible at $v = 4000$ mV/s (Figures 3A and 3C). This indicates an irreversible chemical transformation following electrochemical oxidation to **[1-NO₃]**⁺. Presumably, at faster scan rates the back reduction to **1-NO₃** occurs before chemical decomposition can take place (by an EC mechanism). Though the identity of this decomposition product is not yet known, a possible decomposition route involves loss of NO₂· via homolytic cleavage of the N–O bond of the nitrato ligand, with concurrent one-electron reduction of the cluster. The nature of the oxidized cubane complexes and, specifically, the nature of the electron hole are discussed in the following "Computational Results" section.

In comparison to $Co_4O_4(OAc)_4py_4$, the $[MnCo_3O_4]$ cubanes all require higher applied potentials for oxidation. This effect can be ascribed to the difficulty in removing an electron from the more positively charged $[MnCo_3O_4]^{5+}$ (versus the $[Co_4O_4]^{4+}$) core, and is dramatically illustrated by comparison of the isostructural $[MnCo_3O_4(OAc)_4py_4]^+$ (**[1-py]**⁺) and $Co_4O_4(OAc)_4py_4$ clusters, which shows that **[1-py]**⁺ requires a 1.2 V higher potential for oxidation. Agapie and co-workers have quantified a similar effect for a series of $[MMn_3O_4]$ (M = metal) clusters, for which the redox potentials correlate with the Brønsted acidity of the hydrated M^{n+} ion.[9] A similar effect appears to be operative in the $[MCo_3O_4]$ series. Additionally, it is observed that the ligand bound to Mn(IV) has a strong influence on the redox properties of the core. A redox range of nearly 300 mV is spanned by the simple modulation of electron-donating properties of the ligand bound to Mn(IV).

Spectroscopy

Multimetallic compounds comprising heterometals and/or metals of different oxidation states may be susceptible to complex electronic states due to valence delocalization or tautomerization. Thus, in addition to crystallographic data, spectroscopic data is needed to correctly characterize the valencies of the constituent metals. Preliminary evidence suggested that the Mn and Co valences in the cubane complexes may be localized on their respective ions (Robin–Day class I) as indicated by the absence of an intervalence charge-transfer (IVCT) band in the near-infrared (NIR) spectrum (900–1600 nm) (Figure S1). This suggests that these cubanes exist as either $[Mn^{IV}Co^{III}_3]$ or $[Mn^{III}Co^{IV}Co^{III}_3]$, but probably not $[Mn^{3.25}Co^{3.25}_3]$.

Multifrequency EPR spectroscopic experiments were performed in order to obtain further insight into the electronic structures of complexes **1-OAc**, **1-Cl**, **1-NO₃**, and **[1-py]PF₆**. In general, EPR spectra of Kramers spin systems with $S > 1/2$ are strongly influenced by the relative magnitudes of the axial zero-field splitting (ZFS), D, the transverse ZFS component, E, and the electron Zeeman splitting energy, $h\nu$. Spectra recorded under a weak-field regime (where $D \gg h\nu$) display features whose positions are determined primarily by the E/D ratio. Spectra recorded under an intermediate-field regime (where $D \approx h\nu$) can be exceedingly complicated with the spectral features highly sensitive to small changes in E and/or D. At X-

band (9.4 GHz), the continuous-wave (CW) EPR spectra of complexes **1-OAc**, **1-Cl**, **1-NO₃**, and **[1-py]PF₆** display features whose field positions are consistent with $S = 3/2$ spin systems recorded under the weak-to-intermediate-field regime (Figure 4). For example, the broad positive features centered around 130 mT ($g_{eff} \approx 5$) that are present in each of the spectra arise from the low-field components of the $m_S = -1/2 \leftrightarrow +1/2$ and $m_S = -3/2 \leftrightarrow +3/2$ transitions that are characteristic of $S = 3/2$ spin systems. The spectra are broadened due to a distribution in E and D and by unresolved hyperfine coupling to ^{55}Mn, ^{59}Co, and other nuclei. The EPR spectra of powder samples (see Figure S2) are qualitatively similar but not identical to the frozen-solution spectra, reflecting small differences in molecular structure that likely contribute to a complex distribution of the ZFS parameters.

To gain further insight into the ZFS parameters, we recorded the field-swept pulse EPR spectra of complexes **1-OAc**, **1-Cl**, **1-NO₃**, and **[1-py]PF₆** at D-band (130 GHz) using a Hahn-echo detection sequence ($\pi/2-\tau-\pi-\tau$–echo) (Figure 4). At this higher frequency, $D \ll h\nu$, which results in a sharp, central-field feature corresponding to the $m_S = -1/2 \leftrightarrow +1/2$ transition, as well as broader features corresponding to the $m_S = -3/2 \leftrightarrow -1/2$ and $m_S = +1/2 \leftrightarrow +3/2$ transitions. The breadth of the latter transitions corresponds to D, and their shapes are sensitive to E/D. Thus, analysis of the D-band spectra gives more precise values for D and E than analysis of the relatively complex X-band spectra. The values obtained by spectral simulation of both the X- and D-band spectra show that both D and E are sensitive to ligand substitution at the Mn center, and the magnitudes of the D values (Table 1) are consistent with those observed for other Mn(IV) complexes.[25] The ZFS parameters therefore corroborate the X-ray crystallographic data—particularly the short Mn–ligand distances and the lack of a pseudo-Jahn–Teller axis about the Mn center—as well as the NIR spectroscopic data in the [Mn^{IV}Co^{III}₃] valence assignments for the heterometallic cubane complexes **1-OAc**, **1-Cl**, **1-NO₃**, and **[1-py]PF₆**.

Pulse ENDOR spectra were recorded to assess the validity of a [Mn^{IV}Co^{III}₃] valence assignment. Obtaining pulse ENDOR at D- band rather than at X-band has two important advantages for these complexes: the sharpness of the EPR signal at D-band (particularly the central $m_S = -1/2 \leftrightarrow +1/2$ transition) gives strong ENDOR signal intensity, and relaxation is slower, allowing for magnetic coherence throughout the ENDOR pulse sequence. The spin Hamiltonian (eq 2) contains contributions from the electron Zeeman, nuclear Zeeman, and hyperfine interactions, where μ_B is the Bohr magneton, $\mathbf{B}_0$ is the magnetic field, g is the electronic g-factor, $\mathbf{S}$ is the total electron spin, g_n is the nuclear g-factor, μ_n is the nuclear magnetic moment, $\mathbf{I}$ is the nuclear spin, h is Planck's constant, and $\mathbf{A}$ is the hyperfine coupling constant.

$$H = \mu_B \mathbf{B}_0 \cdot \mathbf{g} \cdot \mathbf{S} - g_n \mu_n \mathbf{B}_0 \cdot \mathbf{I} + h\mathbf{S} \cdot \mathbf{A} \cdot \mathbf{I} \quad (2)$$

Note that nuclear quadrupole contributions for the ^{55}Mn ($I = 5/2$) and ^{59}Co ($I = 7/2$) nuclei are obscured by the ENDOR line width in our spectra (*vide infra*) and are therefore not included in this Hamiltonian. In the strong-field limit, the corresponding energy levels can be written as in eq 3:

$$E/h = \nu_e m_S - \nu_n m_I + A m_S m_I \quad (3)$$

with $\nu_e = g\mu_B B_0/h$ and $\nu_n = g_n\mu_n B_0/h$. For an $S = 3/2$, $I = 1/2$ spin system, $m_S = \pm1/2, \pm3/2$ and $m_I = \pm1/2$, which gives energy levels ($|m_S, m_I\rangle$):

$$\left|\frac{3}{2}, -\frac{1}{2}\right\rangle = \frac{3}{2}\nu_e + \frac{1}{2}\nu_n - \frac{3}{4}A \quad (4)$$

$$\left|\frac{3}{2}, \frac{1}{2}\right\rangle = \frac{3}{2}\nu_e - \frac{1}{2}\nu_n + \frac{3}{4}A \quad (5)$$

$$\left|\frac{1}{2}, -\frac{1}{2}\right\rangle = \frac{1}{2}\nu_e + \frac{1}{2}\nu_n - \frac{1}{4}A \quad (6)$$

$$\left|\frac{1}{2}, \frac{1}{2}\right\rangle = \frac{1}{2}\nu_e - \frac{1}{2}\nu_n + \frac{1}{4}A \quad (7)$$

$$\left|-\frac{1}{2}, -\frac{1}{2}\right\rangle = -\frac{1}{2}\nu_e + \frac{1}{2}\nu_n + \frac{1}{4}A \quad (8)$$

$$\left|-\frac{1}{2}, \frac{1}{2}\right\rangle = -\frac{1}{2}\nu_e - \frac{1}{2}\nu_n - \frac{1}{4}A \quad (9)$$

$$\left|-\frac{3}{2}, -\frac{1}{2}\right\rangle = -\frac{3}{2}\nu_e + \frac{1}{2}\nu_n + \frac{3}{4}A \quad (10)$$

$$\left|-\frac{3}{2}, \frac{1}{2}\right\rangle = -\frac{3}{2}\nu_e - \frac{1}{2}\nu_n - \frac{3}{4}A \quad (11)$$

Application of the NMR selection rules ($m_S = 0$ and $m_I = \pm1$) gives four allowed transitions with frequencies of $\nu_n - \frac{3}{2}A$, $\nu_n - \frac{1}{2}A$, $\nu_n + \frac{1}{2}A$, and $\nu_n + \frac{3}{2}A$. The ordering of

these transitions in the ENDOR spectrum depends on the signs of A and D and the relative magnitudes of A and ν_n. For the strongly coupled case (i.e., $\nu_n < \frac{1}{2}|A|$), the ENDOR spectrum is expected to feature up to four peaks at frequencies given by

$$\nu_1 = \frac{1}{2}|A| - \nu_n \quad (12)$$

$$\nu_2 = \frac{1}{2}|A| + \nu_n \quad (13)$$

$$\nu_3 = \frac{3}{2}|A| - \nu_n \quad (14)$$

$$\nu_4 = \frac{3}{2}|A| + \nu_n \quad (15)$$

where the peaks are separated by $2\nu_n$, $|A| - 2\nu_n$, and $2\nu_n$, respectively.

The Davies ENDOR spectrum of complex **1-Cl** recorded at 4.648 T (Figure 5) shows multiple contributions from ^{55}Mn, ^{59}Co, and ^{1}H nuclei. ENDOR spectra acquired at this field position feature contributions from both the central-field EPR transitions (between the $m_S = \pm 1/2$ energy levels) and outer-manifold EPR transitions (between the $m_S = \pm 1/2$ and $m_S = \pm 3/2$ energy levels). Three of the four ENDOR lines originating from a strongly coupled ^{55}Mn nucleus can be observed over this frequency range. The peaks at 155 and ~265 MHz are well-resolved from the other ENDOR features and correspond to ν_2 and ν_3, respectively; ν_1 is obscured by ^{59}Co ENDOR peaks (*vide infra*), and ν_4 is outside the range of the radiofrequency amplifiers employed in these studies (see the Supporting Information). No nuclear quadrupolar splitting is observed in any of the ^{55}Mn ENDOR peaks, including the relatively narrow ν_2 peak. Spectral simulations of the ν_2 peak show that the largest component of the nuclear quadrupole tensor, Q_{zz}, is less than 1.3 MHz (see Figure S3). By comparison, Q_{zz} for the ^{55}Mn(III) and ^{55}Mn(IV) sites in a dinuclear Mn(III)Mn(IV) complex were determined to be 3.0 and 1.3 MHz, respectively, which further supports a Mn(IV) valence assignment in complex **1-Cl** and the other cubanes described herein.[26]

The ν_3 ^{55}Mn ENDOR peak is in fact composed of two nearly overlapping peaks at 261 and 266 MHz and may be modeled using two slightly different hyperfine couplings. The magnitude of each **A**-tensor may be evaluated by observing that

$$\nu_2+\nu_3=\frac{3}{2}|A| - \nu_{\mathrm{n}}+\frac{1}{2}|A|+\nu_{\mathrm{n}}=2|A| \quad (16)$$

which gives $2|A| = 155 + 266$ MHz, or $|A| \approx 210$ MHz for the high-frequency component of the ν_3 peak, and $2|A| = 155 + 261$ MHz, or $|A| \approx 208$ MHz for the low-frequency component of the ν_3 peak. We attribute the two slightly different $A(^{55}\mathrm{Mn})$ hyperfine tensors to two slightly different forms (e.g., conformations or rotamers) of complex **1-Cl** in the frozen solution. The intensities of the two components are not equal and vary with field (Figure 5), which suggests that the two components have slightly different ZFS parameters. Using these guiding assumptions, the $^{55}\mathrm{Mn}$ ENDOR were simulated using the following parameters: component 1 (50%) with $D = 0.16$ cm^{-1}, $E/D = 0.15$, and $A(^{55}\mathrm{Mn1}) = -210.5$ MHz; component 2 (50%) with $D = 0.2$ cm^{-1}, $E/D = 0.1$, and $A(^{55}\mathrm{Mn2}) = -207$ MHz.

The sign of $A(^{55}\mathrm{Mn})$ does not affect the frequencies of the $^{55}\mathrm{Mn}$ ENDOR peaks, but it does affect their relative intensities. In general, the intensities of the ENDOR peaks will be strongly influenced by the Boltzmann population distribution of the electron spin states, with the $m_S = -3/2$ state being most populated and the $m_S = +3/2$ state being least populated for $D > 0$ (as is most commonly observed for mononuclear Mn(IV)).[27,28] As such, neglecting other factors, ENDOR transitions in the $m_S = -3/2 \leftrightarrow -1/2$ manifold are expected to be more intense than ENDOR transitions in the $m_S = +1/2 \leftrightarrow +3/2$ manifold. For $A < 0$, ν_3 would correspond to the NMR transition in the $m_S = -3/2 \leftrightarrow -1/2$ manifold (Figure 6A) and should therefore give rise to a strong ENDOR signal at low temperature. On the other hand, for $A > 0$, ν_3 would correspond to the NMR transition in the $m_S = +1/2 \leftrightarrow +3/2$ manifold and would be expected to give rise to a relatively weaker ENDOR signal at low temperature. Spectral simulation (Figure 6B) confirms these expectations, showing that, for $A > 0$, the ν_3 peak in the ENDOR spectrum recorded at 4.648 T is expected to be substantially weaker than the ν_1 and ν_2 peaks, with almost vanishing intensity at the temperatures employed in this study (5.2 K). However, the experimental spectrum shows a strong ν_3 peak, and the features attributable to $^{55}\mathrm{Mn}$ hyperfine coupling can be readily simulated using negative hyperfine tensors: $A(^{55}\mathrm{Mn1}) = -210.5$ and $A(^{55}\mathrm{Mn2}) = -207$ MHz. Overall, the observed $^{55}\mathrm{Mn}$ ENDOR peaks can be assigned as given in Table S1.

The features between 33 and 84 MHz in the ENDOR spectra of complex **1-Cl** (Figure 5) arise from coupled $^{59}\mathrm{Co}$ nuclei. In the weak-coupling regime (i.e., $|\nu_{\mathrm{n}}|<\frac{3}{2}|A|$), the NMR transitions have energies $\nu_{\mathrm{n}} - \frac{3}{2}|A|, \nu_{\mathrm{n}} - \frac{1}{2}|A|, \nu_{\mathrm{n}}+\frac{1}{2}|A|$, and $\nu_{\mathrm{n}}+\frac{3}{2}|A|$ with the four peaks in the ENDOR spectrum centered at ν_{n} and separated by $|A|$. Spectral simulation of the complex **1-Cl** ENDOR spectra gives three $A(^{59}\mathrm{Co})$ tensor values of 21, 17, and 14 MHz. The difference in magnitude of the three $^{59}\mathrm{Co}$ couplings points to slight differences in the chemical environment of each Co center induced by the asymmetry of the Mn coordination environment. As for $A(^{55}\mathrm{Mn})$, the relative intensities of the observed ENDOR transitions are strongly affected by the signs of the $A(^{59}\mathrm{Co})$ tensors, and simulations of the $^{59}\mathrm{Co}$ ENDOR lines are only satisfactory when positive $A(^{59}\mathrm{Co})$ values are employed (still assuming $D >$

0). Overall, the stronger [55]Mn hyperfine coupling supports the proposal that complex **1-Cl** is composed of an $S = 3/2$ Mn(IV) center with three $S = 0$ Co(III) centers, and the weaker—but still significant—[59]Co hyperfine coupling points to the covalency of the $[MnCo_3O_4]^{5+}$ core. Moreover, the Davies ENDOR spectra of **1-Cl** and **1-OAc** are strikingly similar (see Figure S4), which suggests that the hyperfine parameters of **1-Cl** and **1-OAc** are representative of each of the MnCo_3O_4 cubanes studied herein.

We also employed electron–electron double resonance-detected NMR (EDNMR) to study the hyperfine interactions of **1-OAc**. Whereas ENDOR experiments use radiofrequency radiation of variable frequency to drive NMR transitions, EDNMR experiments use a high-turning-angle (HTA) pulse of variable microwave frequency to simultaneously drive both the EPR and NMR transitions.[29,30] EDNMR spectra may typically be acquired more rapidly than their corresponding Davies ENDOR spectra, though EDNMR spectra suffer from broader line shapes and may also display combination bands and overtones, thereby producing feature-rich, complex spectra. Each of these attributes is observed in the EDNMR spectra of **1-OAc** (Figure 7 for data acquired at 4.648 mT and Figure S5 for data acquired at additional fields). Three relatively broad low-frequency peaks at 39, 57, and 77 MHz correspond to the more complex set of [59]Co hyperfine peaks observed in this region in the Davies ENDOR (Figures 6B and 7). The ν_2 [55]Mn hyperfine line is also observed, along with its double- and triple-quantum overtones. Combination bands of these [55]Mn lines and the 39 MHz [59]Co line are also observed and can be seen as splitting of the [55]Mn lines. The presence of multiple overlapping overtones and combination bands preclude an assignment of every feature in the EDNMR spectra. Nonetheless, these data further support our hyperfine assignments for **1-OAc** and for this series of complexes more generally.

Magnetism

DC magnetic susceptibility measurements were performed under an applied magnetic field of 0.1 T for compounds **1-OAc** and **[1-py]PF_6** (Figure 8). Both **1-OAc** and **[1-py]PF_6** exhibit room temperature $\chi_M T$ products consistent with the value expected for the isotropic $S = 3/2$ spin associated with Mn(IV). These values are 1.86 emu·K/mol and 1.87 emu·K/mol for **1-OAc** and **[1-py]PF_6**, respectively, compared to the expected value of 1.876 emu·K/mol. Next, variable temperature magnetization data were collected at applied magnetic fields of 1–7 T and temperatures ranging from 2 to 15 K in order to investigate the magnetic anisotropy in these systems (Figures S7 and S8). Slight non-superimposability of the isofield lines when plotted vs H/T indicated that **1-OAc** and **[1-py]PF_6** display some magnetic anisotropy, presumably determined by the specific coordination environment of the Mn(IV) in each system, in agreement with EPR measurements. Given that SQUID magnetometry was performed on samples in the solid state, while EPR data was obtained with samples in comparatively dilute frozen solutions, EPR should provide the best estimates of D and E for the Mn(IV) centers in these molecules, as the data should be unaffected by intermolecular magnetic couplings. Modeling of the M vs H data for **1-OAc** using the zero-field splitting parameters determined by EPR shows reasonable, though not perfect, agreement (Figure S9). Similar modeling for **[1-py]PF_6** shows poor agreement, ascribed to the presence of intermolecular magnetic coupling with a magnitude comparable to that of the zero-field splitting parameters for **[1-py]PF_6** (Figure S10). The presence of significant

antiferromagnetic intermolecular interactions for **[1-py]PF$_6$** is supported by the observation of a low saturation magnetization of 2.3 μ_B at 7 T and 2 K, compared to the 3 μ_B expected for an isolated $S = 3/2$ center.

Computational Results

Density functional theory (DFT) calculations corroborated the localization of valence within the clusters. Mulliken spin densities for the DFT-optimized structure of **1-OAc** demonstrated three unpaired spins residing mainly on the Mn ion, and therefore a Mn(IV) assignment (Figure 6A). No significant spin density was found on the Co ions, consistent with the expected t_{2g}^6 configuration for Co(III), the strong ^{55}Mn hyperfine coupling observed in the ENDOR and EDNMR spectra, and the magnetometry results.

The oxidized cubane, **[1-OAc]$^+$**, was also subjected to DFT calculations, in order to address the question of whether the electron is lost from Mn(IV) or Co(III) during oxidation. The calculation first revealed that the quintet and triplet spin states are essentially degenerate (differing only in whether or not the Co(IV) center is ferromagnetically or antiferromagnetically coupled to the Mn spins) as there is minimal direct electronic coupling of the unpaired spins on the Mn with the Co centers. The geometries are negligibly different between the different spin states. From the Mulliken and LOBA,[31] one of the Co(III) centers is oxidized to a Co(IV) center. Again, DFT suggests a ground state with localized Mn(IV) and Co(IV) valencies (Figure 9A). Significant bond length changes also occur upon oxidation (Figure 9B). For **[1-OAc]$^+$**, there is a marked contraction of the Mn–OAc bond even though the oxidation state of Mn does not change upon oxidation of the cluster. Simultaneously, the three Co(IV)–μ_3-O bonds contract significantly, while the other Co(III)–μ_3-O bonds elongate to compensate. Thus, the oxidation at a distal cobalt ion propagates structural changes throughout the entire cluster, yet, notably, the nature of the ligand at Mn(IV) modulates the redox potential of the distal Co ion (*vide supra*). These results demonstrate a cooperative communication between the Mn and Co ions within the cluster. Calculations on **[1-Cl]$^+$** and **[1-NO$_3$]$^+$** showed nearly identical distribution of spins to that of **[1-OAc]$^+$** (Supporting Information). This result suggests that there is a strong preference for oxidizing the Co(III) ions over the Mn(IV) ion.

CONCLUSIONS

A heterometallic oxo-cubane with Mn and Co ions, supported only by simple carboxylate and pyridine ligands, has been rationally synthesized by a one-step method. This synthesis demonstrates that complex heterometallic clusters can be made in a designed manner with biologically relevant ligands. The MnCo$_3$O$_4$(OAc)$_5$py$_3$ cubane, **1-OAc**, is the first example of a Mn–Co oxo-cubane. Derivatives of this cubane were accessed by postsynthetic treatment of **1-OAc** with different reagents, producing homologues with Cl$^-$, NO$_3$$^-$, and OTs$^-$ functionalities. A cationic [MnCo$_3$O$_4$(OAc)$_4$py$_4$]$^+$ derivative was also made, and this complex is isostructural with the well-studied cobalt cubane OER catalyst, Co$_4$O$_4$(OAc)$_4$py$_4$. Thus, comparisons of these related complexes may give insights into cooperative effects associated with heterobimetallic catalysts. Moreover, the [MnCo$_3$O$_4$]

clusters are water-stable, and most are also water-soluble, which will allow future studies of water oxidation chemistry.

Structural, spectroscopic, and magnetic studies of the $[MnCo_3O_4]$ clusters support a valence-localized electronic structure with an $S = 3/2$ Mn(IV) center and three $S = 0$ Co(III) centers. Although our data favor a $[Mn^{IV}Co^{III}_3]$ rather than a $[Mn^{III}Co^{IV}Co^{III}_2]$ electronic structure, the non-negligible ^{59}Co hyperfine coupling observed by ENDOR and EDNMR spectroscopy indicates significant covalency of the $[MnCo_3O_4]^{5+}$ core as has been suggested for $[Co_4O_4]^{5+}$ cubanes.[11,32] In addition, DFT suggests that oxidation of the cubanes occurs from a Co(III) site rather than the Mn(IV) site, yet the structural consequences of the oxidation are transmitted throughout the cluster. While the ligand-exchange chemistry occurs at the Mn site, the redox chemistry occurs in the remaining $[Co_3O_4]$ subcluster. Thus, the $[Co_3O_4]$ moiety is conceptually a redox-active ligand for manganese. Meanwhile, the ligand on Mn modulates the redox potentials of the distal Co centers, thus demonstrating cooperativity between Mn and Co. Such cooperativity may be operative in Mn-doped CoO_x, as well: the Mn sites are better suited to generate terminal-oxo moieties necessary for O–O bond formation,[33,34] while the Co sites help store electron-hole equivalents. This modulation of reactivity by distal redox changes was also recently observed in a molecular $[Fe_4O]$ cluster reported by Agapie and co-workers,[35] and could be a more general phenomenon in cluster chemistry.

Supplementary Material

Refer to Web version on PubMed Central for supplementary material.

Acknowledgments

References

1. Lewis NS, Nocera DG. Proc. Natl. Acad. Sci. U. S. A. 2006; 103:15729–15735. [PubMed: 17043226]

2. Burke MS, Kast MG, Trotochaud L, Smith AM, Boettcher SW. J. Am. Chem. Soc. 2015; 137:3638–3648. [PubMed: 25700234]

3. Trotochaud L, Young SL, Ranney JK, Boettcher SW. J. Am. Chem. Soc. 2014; 136:6744–6753. [PubMed: 24779732]

4. Song F, Hu X. J. Am. Chem. Soc. 2014; 136:16481–16484. [PubMed: 25380057]

5. Li D, Baydoun H, Verani CN, Brock SL. J. Am. Chem. Soc. 2016; 138:4006–4009. [PubMed: 26972408]

6. Umena Y, Kawakami K, Shen J-R, Kamiya N. Nature. 2011; 473:55–60. [PubMed: 21499260]

7. Rhee K-H, Morris EP, Barber J, Kühlbrandt W. Nature. 1998; 396:283–286. [PubMed: 9834037]

8. Kanady JS, Tsui EY, Day MW, Agapie T. Science. 2011; 333:733–736. [PubMed: 21817047]

9. Tsui EY, Agapie T. Proc. Natl. Acad. Sci. U. S. A. 2013; 110:10084–10088. [PubMed: 23744039]

10. Nguyen AI, Ziegler MS, Oña-Burgos P, Sturzbecher-Hohne M, Kim W, Bellone DE, Tilley TD. J. Am. Chem. Soc. 2015; 137:12865–12872. [PubMed: 26390993]

11. McAlpin JG, Stich TA, Ohlin CA, Surendranath Y, Nocera DG, Casey WH, Britt RD. J. Am. Chem. Soc. 2011; 133:15444–15452. [PubMed: 21913664]

12. Mukherjee S, Stull JA, Yano J, Stamatatos TC, Pringouri K, Stich TA, Abboud KA, Britt RD, Yachandra VK, Christou G. Proc. Natl. Acad. Sci. U. S. A. 2012; 109:2257–2262. [PubMed: 22308383]

13. Zhang C, Chen C, Dong H, Shen J-R, Dau H, Zhao J. Science. 2015; 348:690–693. [PubMed: 25954008]

14. Smith PF, Hunt L, Laursen AB, Sagar V, Kaushik S, Calvinho KUD, Marotta G, Mosconi E, De Angelis F, Dismukes GC. J. Am. Chem. Soc. 2015; 137:15460–15468. [PubMed: 26593692]

15. Lis T. Acta Crystallogr., Sect. B: Struct. Crystallogr. Cryst. Chem. 1980; 36:2042–2046.

16. Long D-L, Burkholder E, Cronin L. Chem. Soc. Rev. 2007; 36:105–121. [PubMed: 17173149]

17. Beattie JK, Hambley TW, Klepetko JA, Masters AF, Turner P. Polyhedron. 1998; 17:1343–1354.

18. Chakrabarty R, Bora SJ, Das BK. Inorg. Chem. 2007; 46:9450–9462. [PubMed: 17910439]

19. Kanady JS, Mendoza-Cortes JL, Tsui EY, Nielsen RJ, Goddard WA, Agapie T. J. Am. Chem. Soc. 2013; 135:1073–1082. [PubMed: 23241061]

20. Kanady JS, Tran R, Stull JA, Lu L, Stich TA, Day MW, Yano J, Britt RD, Agapie T. Chem. Sci. 2013; 4:3986–3996. [PubMed: 24163730]

21. Shinagawa T, Garcia-Esparza AT, Takanabe K. Sci. Rep. 2015; 5:13801. [PubMed: 26348156]

22. Tsui EY, Day MW, Agapie T. Angew. Chem., Int. Ed. 2011; 50:1668–1672.

23. Ullman AM, Liu Y, Huynh M, Bediako DK, Wang H, Anderson BL, Powers DC, Breen JJ, Abruña HD, Nocera DG. J. Am. Chem. Soc. 2014; 136:17681–17688. [PubMed: 25407218]

24. Bordwell FG. Acc. Chem. Res. 1988; 21:456–463.

25. Zlatar M, Gruden M, Vassilyeva OY, Buvaylo EA, Ponomarev AN, Zvyagin SA, Wosnitza J, Krzystek J, Garcia-Fernandez P, Duboc C. Inorg. Chem. 2016; 55:1192–1201. [PubMed: 26745448]

26. Randall DW, Sturgeon BE, Ball JA, Lorigan GA, Chan MK, Klein MP, Armstrong WH, Britt RD. J. Am. Chem. Soc. 1995; 117:11780–11789.

27. Duboc C. Chem. Soc. Rev. 2016; 45:5834–5847. [PubMed: 27508279]

28. Leto DF, Massie AA, Colmer HE, Jackson TA. Inorg. Chem. 2016; 55:3272–3282. [PubMed: 27002928]

29. Schosseler P, Wacker T, Schweiger A. Chem. Phys. Lett. 1994; 224:319–324.

30. Cox N, Lubitz W, Savitsky A. Mol. Phys. 2013; 111:2788–2808.

31. Thom AJW, Sundstrom EJ, Head-Gordon M. Phys. Chem. Chem. Phys. 2009; 11:11297–11304. [PubMed: 20024398]

32. Hadt RG, Hayes D, Brodsky CN, Ullman AM, Casa DM, Upton MH, Nocera DG, Chen LX. J. Am. Chem. Soc. 2016; 138:11017–11030. [PubMed: 27515121]

33. Gao Y, Åkermark T, Liu J, Sun L, Åkermark B. J. Am. Chem. Soc. 2009; 131:8726–8727. [PubMed: 19496534]

34. Betley TA, Wu Q, Van Voorhis T, Nocera DG. Inorg. Chem. 2008; 47:1849–1861. [PubMed: 18330975]

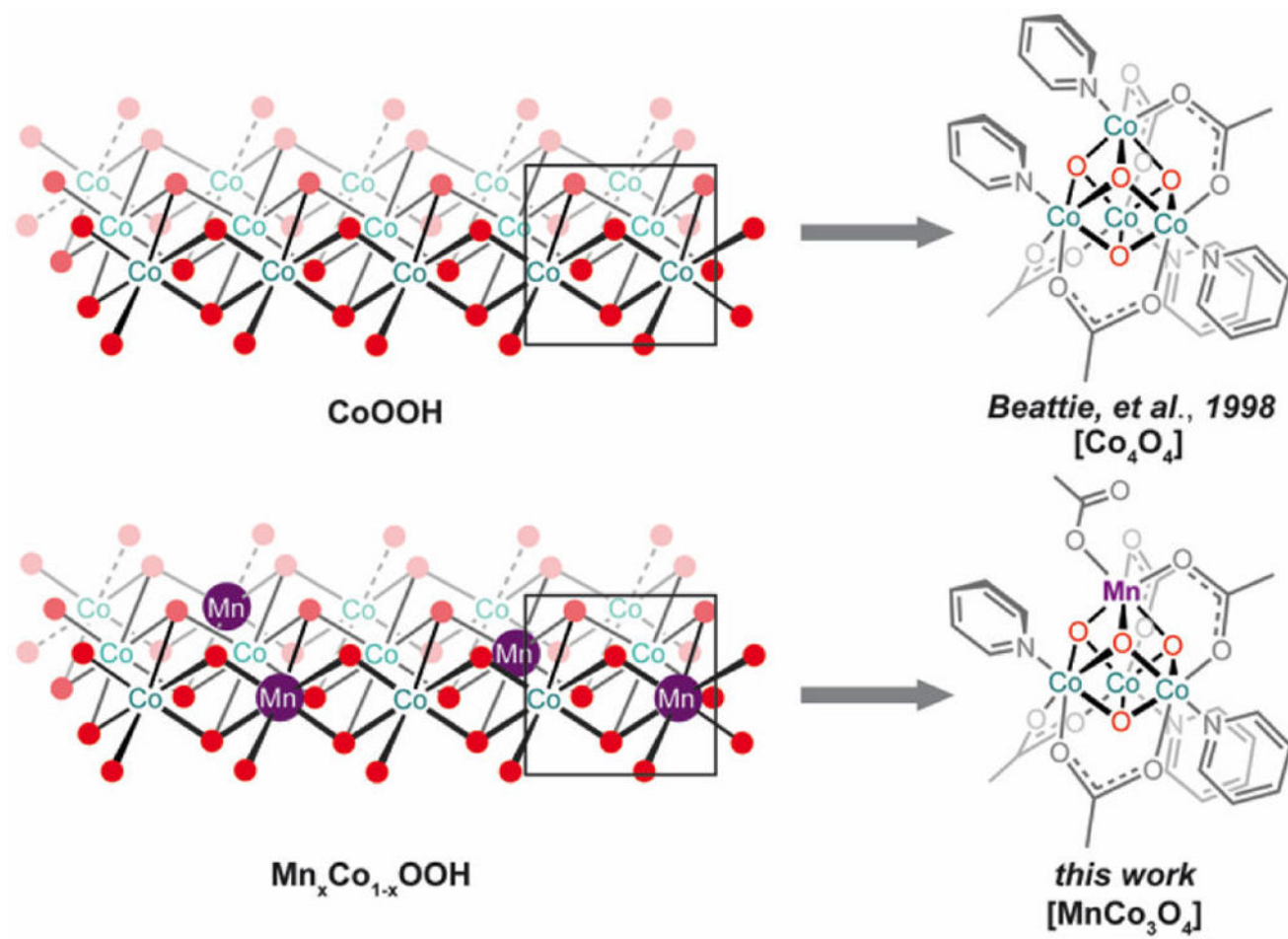35. de Ruiter G, Thompson NB, Lionetti D, Agapie T. J. Am. Chem. Soc. 2015; 137:14094–14106. [PubMed: 26390375]

Figure 1.
Comparison of models for cobalt oxyhydroxide and manganese-doped-cobalt oxyhydroxide.
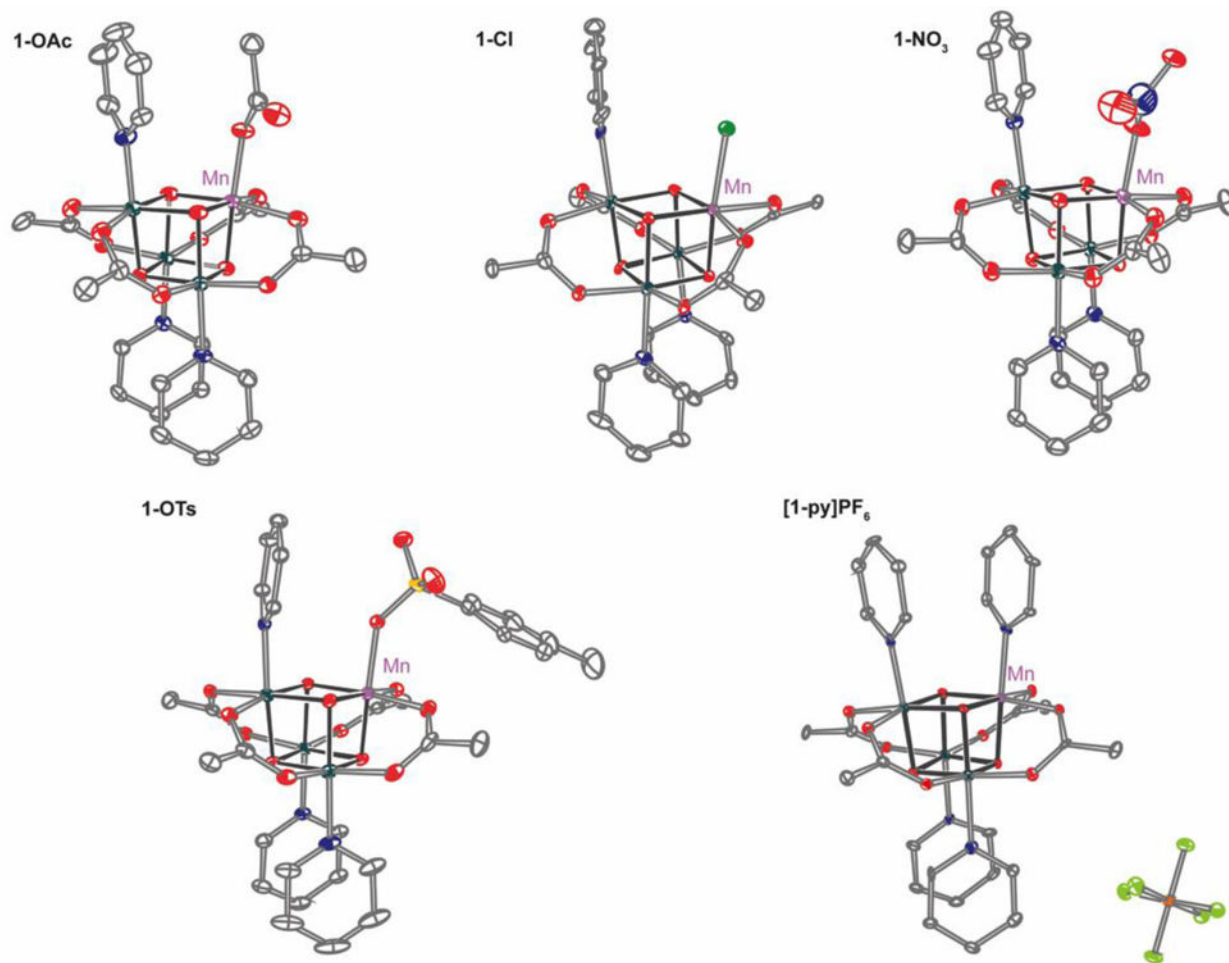
Figure 2.
X-ray crystal structures of [MnCo₃O₄] cubanes. Thermal ellipsoids are shown at 30% probability. Hydrogen atoms and solvent molecules were removed for clarity.
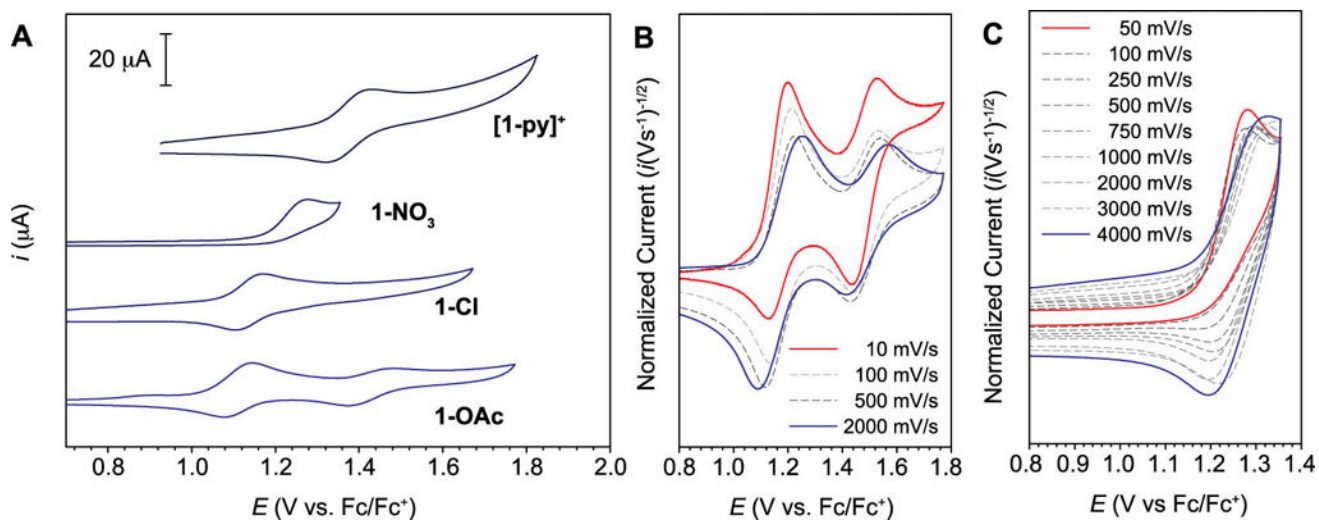
Figure 3.
Electrochemical data. (A) Cyclic voltammograms of cubane complexes ($v = 100$ mV/s, 0.1 M ^{n}Bu$_4$NPF$_6$ supporting electrolyte in MeCN, except for **1-NO$_3$** which was in CH$_2$Cl$_2$). (B) Scan rate dependence of **1-OAc**. (C) Scan rate dependence of **1-NO$_3$**.
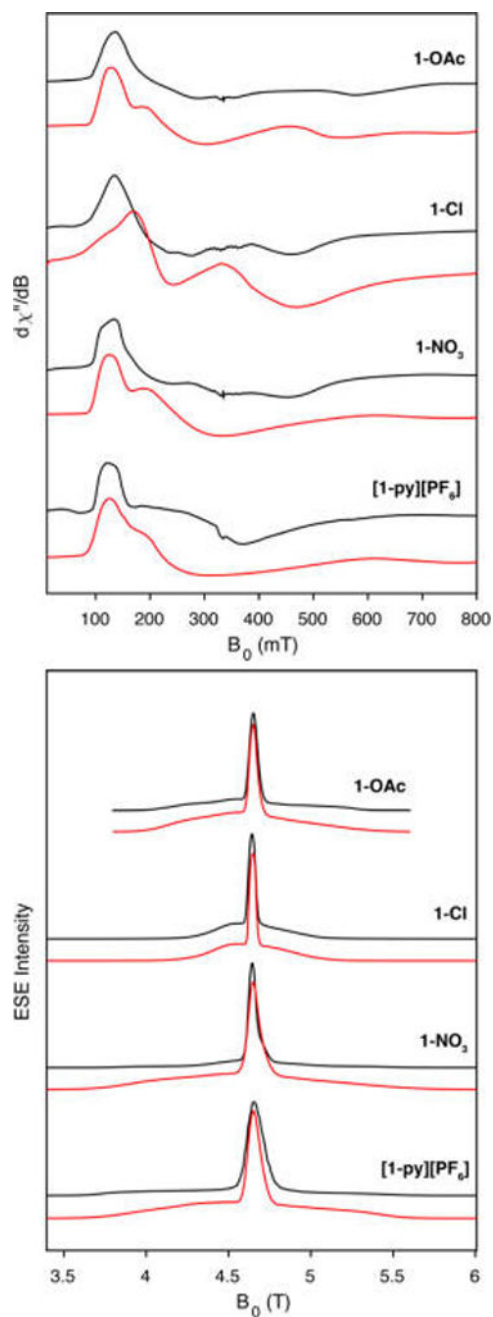
Figure 4.
EPR spectra of cubanes in frozen solutions 1:1 CH_2Cl_2:toluene. (Top panel) X-band (9.4 GHz) at 6 K. (Bottom panel) D-band (130 GHz) at 7 K (except 5 K for **1-OAc**). Data, black; simulations, red.
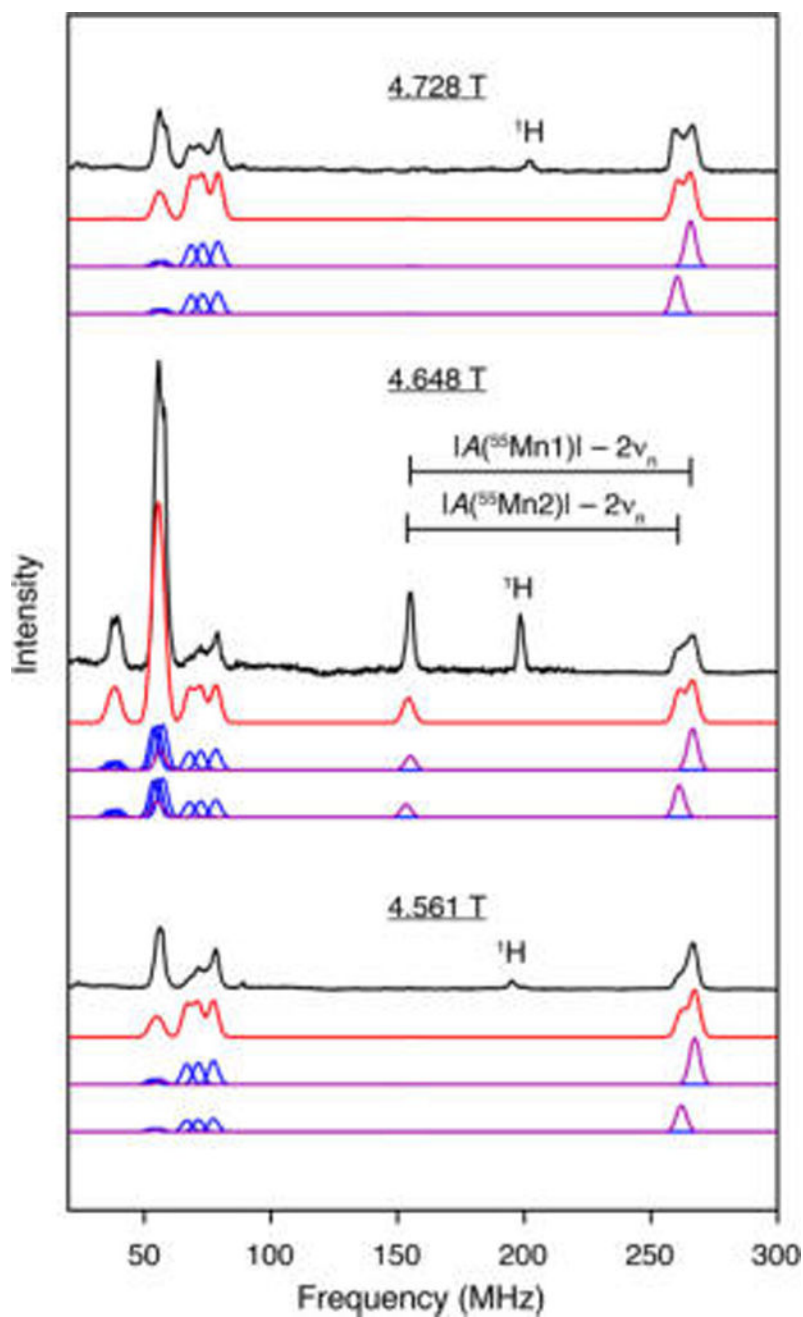
Figure 5.
Davies ENDOR spectra of complex **1-Cl** recorded at 130 GHz and 5.2 K using the following pulse parameters: $\pi/2 = 37.5$ ns, $\pi = 75$ ns, π(RF) $= 2.5$ μs, $\tau = 300$ ns. Four traces are shown for each field position and correspond to (top to bottom) data (black), full simulation (red), component 1 simulation (Mn1 contributions in purple, Co contributions in blue), and component 2 simulation (Mn2 contributions in purple, Co contributions in blue). The full simulation was computed by adding the spectral contributions of components 1 (50%) and 2 (50%).
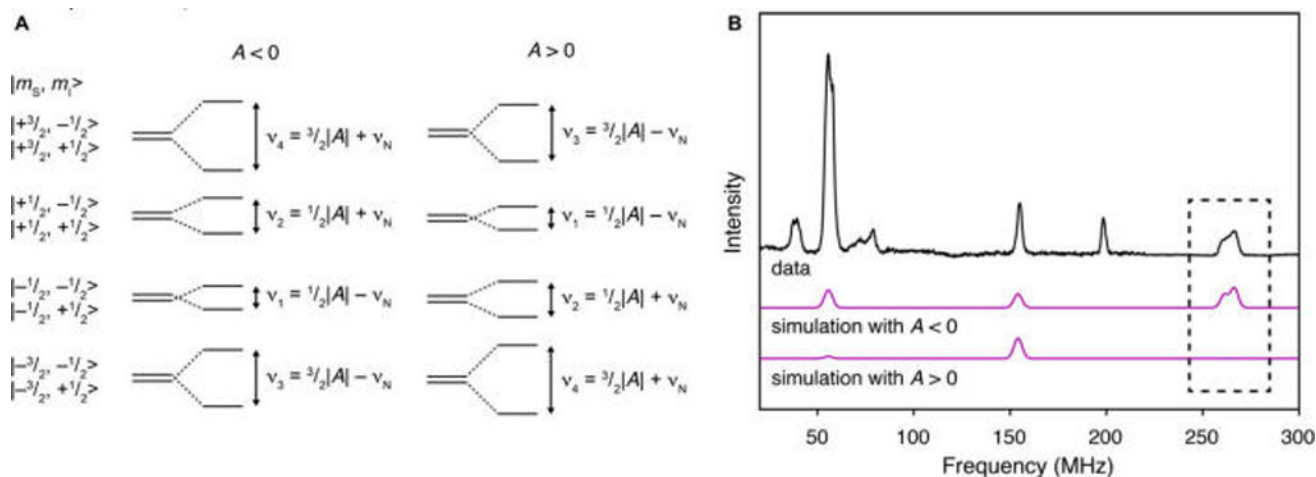
Figure 6.
(A) Energy-level diagram showing how the eight energy levels derived from an $S = 3/2$, $I = 1/2$ spin system are perturbed by hyperfine coupling with a strongly coupled, $I = 1/2$ nucleus. The ordering of the frequencies depends on the sign of A. It is assumed that $D > 0$. (B) D-band ENDOR spectrum of complex **1-Cl** recorded at 4.648 T (top, black; reproduced from Figure 5), and simulation of the ^{55}Mn hyperfine contributions with $A(^{55}Mn1) = -210.5$ MHz and $A(^{55}Mn2) = -207$ MHz (middle, purple) or $A(^{55}Mn1) = 210.5$ MHz and $A(^{55}Mn2) = 207$ MHz (bottom, purple). The region highlighted by the dashed box shows the ν_3 feature that is present in the experimental spectrum and in the middle trace but not in the bottom trace.
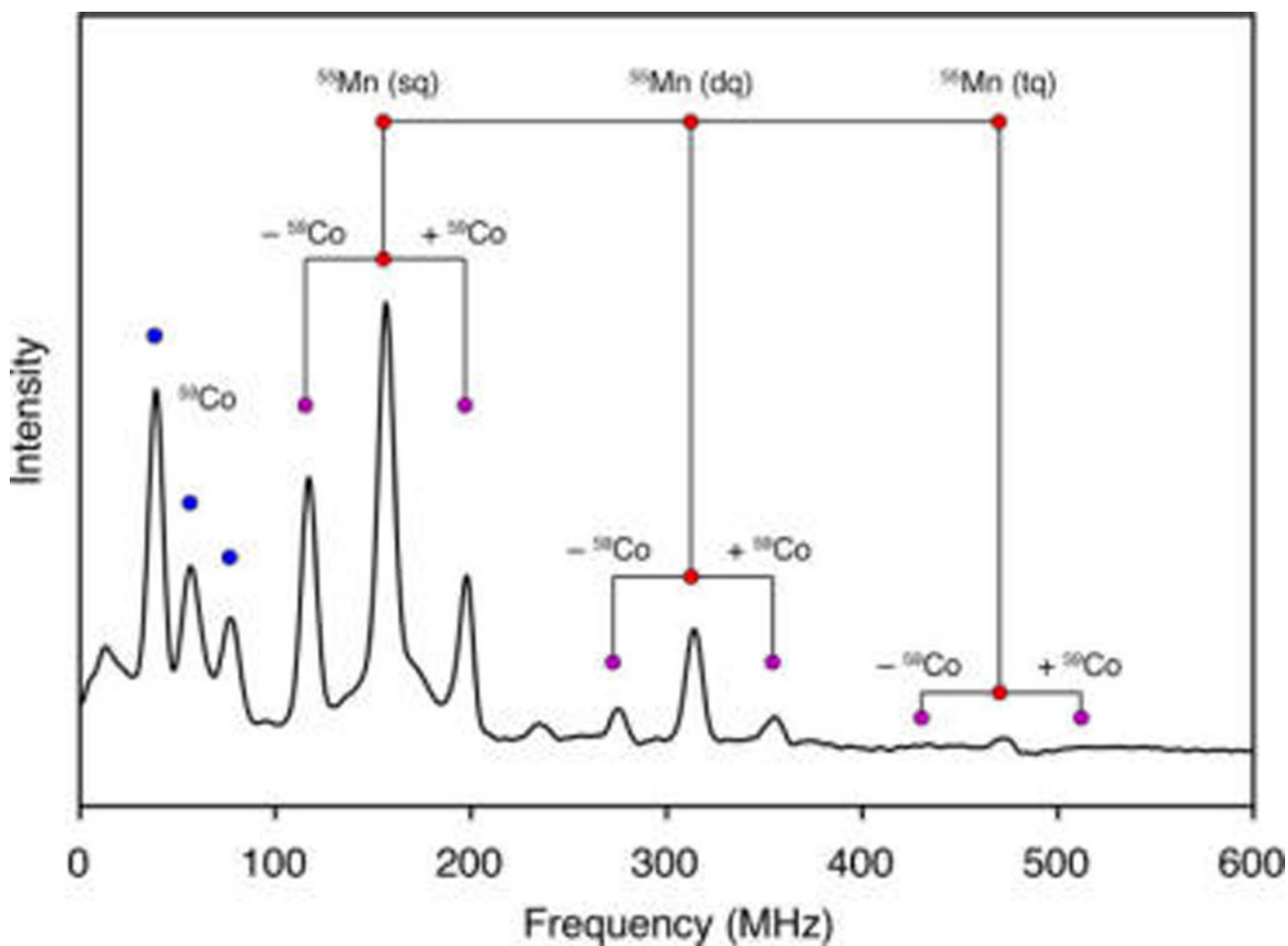
Figure 7.
EDNMR spectra of **1-OAc** recorded at 4.648 mT, 130 GHz, and 5.2 K with an HTA pulse length of 10 μs. Selected assignments shown for ^{59}Co coupling (blue), ^{55}Mn coupling (red), and ^{55}Mn ± ^{59}Co combination bands (purple). sq = single quantum, dq = double quantum, tq = triple quantum. The HTA pulse length dependence on the spectral features is shown in Figure S6.
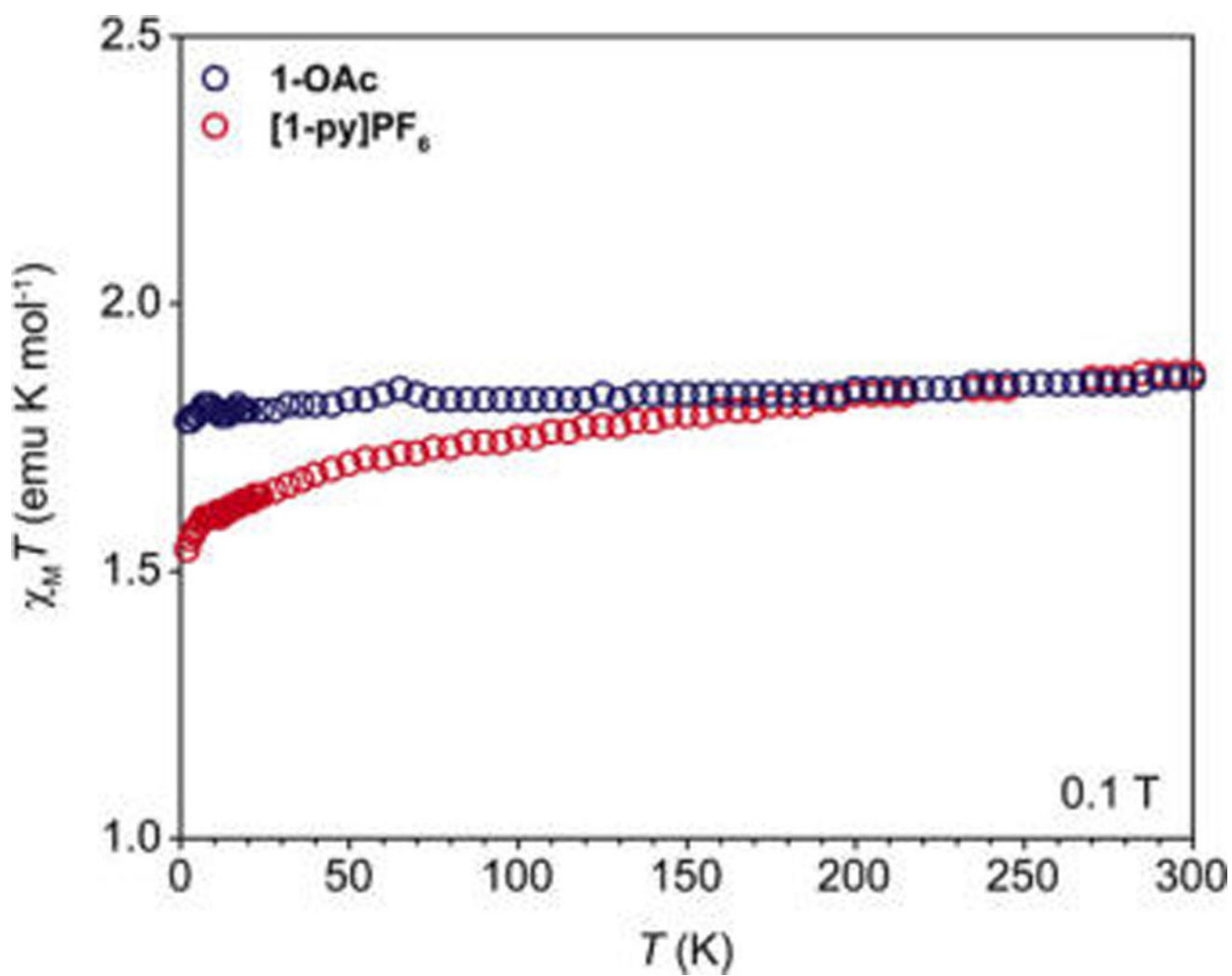
Figure 8.
Solid-state magnetic susceptibility times temperature data for **1-OAc** and **[1-py]PF₆**.
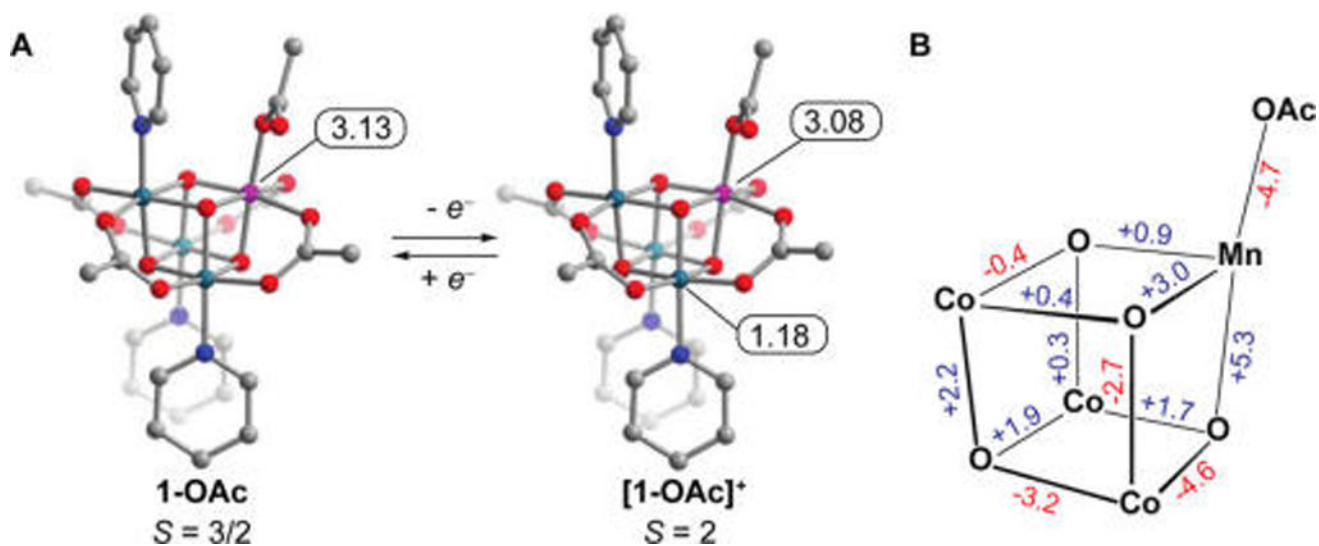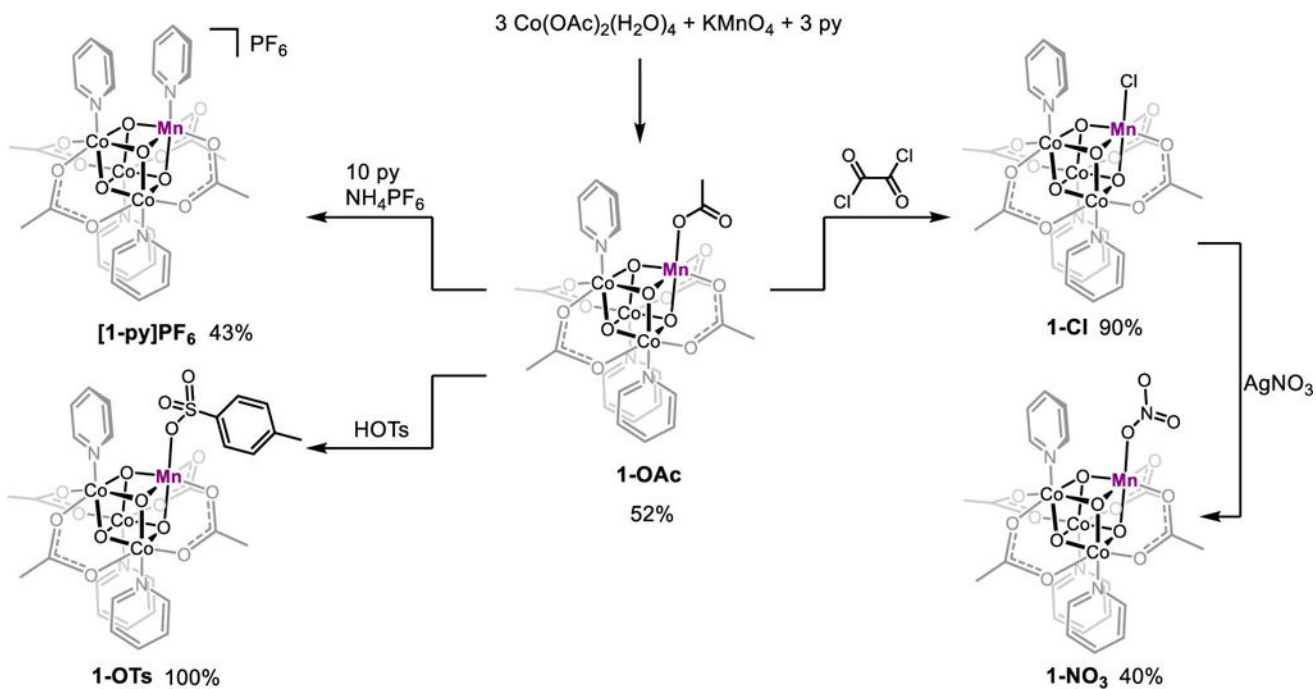
Figure 9.
(A) Unpaired Mulliken spin densities for **1-OAc** and **[1-OAc]⁺** from DFT calculations. Atoms not indicated have spin densities near zero. For **1-OAc**: Co1 = 0.058, Co2 = 0.038, Co3 = −0.014. For **[1-OAc]⁺**: Co2 = 0.052, Co3 = −0.022. (B) Cubane bond distance differences (pm) upon oxidation to **[1-OAc]⁺**.

Scheme 1.
Synthesis of $[MnCo_3O_4]^{5+}$ Congeners

Author Manuscript

Table 1

Mn-ZFS Parameters Determined by EPR Spectroscopy

cluster	D (cm^{-1})^a	E/D^a
1-OAc	0.29	0.24
1-Cl (50%)^b	0.16	0.15
1-Cl (50%)^b	0.20	0.10
1-NO₃	0.40	0.27
[1-py]PF₆	0.44	0.32

^{a}The estimated uncertainty based on the simulations is ±0.02 cm^{-1} for D and ±0.05 for E/D.

^{b}The most satisfactory fits for the EPR and Davies ENDOR spectra of **1-Cl** were obtained by fitting two components in a 1:1 ratio.